Extreme-ultraviolet phase-shifting point-diffraction interferometer: a wave-front metrology tool with subangstrom reference-wave accuracy

Patrick P. Naulleau, Kenneth A. Goldberg, Sang H. Lee, Chang Chang, David Attwood, and Jeffrey Bokor

The phase-shifting point-diffraction interferometer (PS/PDI) was recently developed and implemented at Lawrence Berkeley National Laboratory to characterize extreme-ultraviolet (EUV) projection optical systems for lithography. Here we quantitatively characterize the accuracy and precision of the PS/PDI. Experimental measurements are compared with theoretical results. Two major classes of errors affect the accuracy of the interferometer: systematic effects arising from measurement geometry and systematic and random errors due to an imperfect reference wave. To characterize these effects, and hence to calibrate the interferometer, a null test is used. This null test also serves as a measure of the accuracy of the interferometer. We show the EUV PS/PDI, as currently implemented, to have a systematic error-limited reference-wave accuracy of 0.0028 waves ($\lambda/357$ or 0.038 nm at $\lambda = 13.5$ nm) within a numerical aperture of 0.082.

OCIS codes: 120.3180, 260.7200, 220.3740.

1. Introduction

Wave-front metrology is an essential tool for the development of diffraction-limited extreme-ultraviolet (EUV) lithographic optical systems. Because these systems use resonant-stack, reflective multilayer-coated optics,[1] performing the wave-front measurement at the intended operational wavelength is crucial to measuring coating-induced wave-front errors. EUV lithographic systems require fabrication tolerances of the order of 0.02 waves rms (<0.3-nm rms at a wavelength of 13.5 nm).[2] Such tolerances place extremely high demands on the at-wavelength interferometric testing, which must provide a measurement accuracy of the order of 0.01 waves ($\lambda/100$ or 0.1 nm). The phase-shifting point-diffraction interferometer (PS/PDI),[3–6] recently developed and implemented at Lawrence Berkeley National Laboratory, was designed to achieve this accuracy. At-wavelength interferometric measurement of reflective EUV optical systems has also been reported with use of lateral-shearing interferometry[7] and with Foucault and Ronchi testing.[8]

The two primary sources of measurement error that limit the accuracy of the PS/PDI are imperfections in the reference wave generated by diffraction from the image-plane pinhole and systematic effects that arise from the geometry of the system. Those systematic geometric effects that can be measured in a calibration test are removable. The reference-pinhole-induced errors, however, are much more difficult to remove through calibration, because they depend on the shape and position of the reference pinhole and on the aberrations present in the test optic; however, the portion of these errors that varies randomly as a function of reference pinhole position can be suppressed through averaging.

To characterize the errors described above, and hence calibrate the PS/PDI, a null test may be employed. Analogous to Young's two-slit experiment, a null test can be performed on the PS/PDI by placement of a two-pinhole *null mask* in the image plane.[6] In the null-test case two reference waves are generated by diffraction from the image-plane mask, creating a fringe pattern (interferogram) in the far field

P. P. Naulleau (pnaulleau@lbl.gov), K. A. Goldberg, S. H. Lee, C. Chang, D. Attwood, and J. Bokor are with the Center for X-Ray Optics, Lawrence Berkeley National Laboratory, Berkeley, California 94720. S. H. Lee, C. Chang, D. Attwood, and J. Bokor are also with the Department of Electrical Engineering and Computer Sciences, University of California, Berkeley, Berkeley, California 94720.

Received 17 May 1999; revised manuscript received 16 August 1999.

0003-6935/99/357252-12$15.00/0

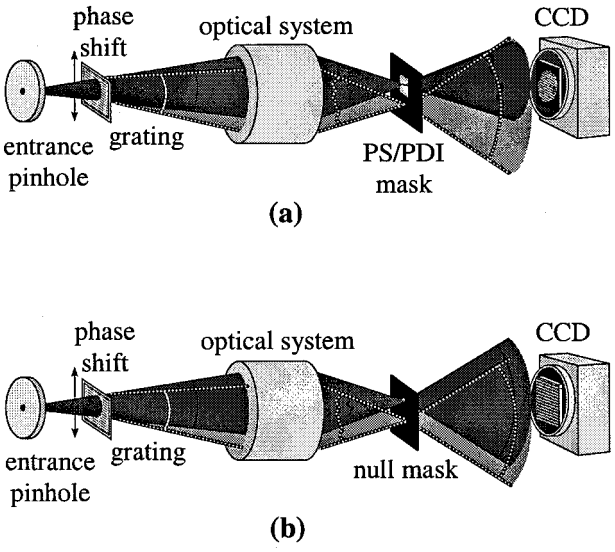

Fig. 1. Schematic of the PS/PDI in (a) the conventional operation configuration and (b) the null-test configuration.

of the mask. Aberrations measured from this null-mask interferogram are indicative of the systematic and random errors in the interferometer. Here we describe and demonstrate a null-test procedure applicable to any implementation of the PS/PDI.

2. Phase-Shifting Point-Diffraction Interferometer Description

The PS/PDI is briefly described here; a more complete description has been previously published.[3–6] The PS/PDI is a variation of the conventional point-diffraction interferometer[9,10] in which a transmission grating has been added to greatly improve the optical throughput of the system and to add phase-shifting capability. In the PS/PDI [Fig. 1(a)], the optical system under test is coherently illuminated by a spherical wave generated by diffraction from a pinhole placed in the object plane. To guarantee the quality of the spherical-wave illumination, the pinhole diameter is chosen to be several times smaller than the resolution limit of the optical system. A grating placed either before or after the test optic is used to split the illuminating beam, creating the required test and reference beams. A mask [the PS/PDI mask in Fig. 1(a)] is placed in the image plane of the optical system under test to block the unwanted diffracted orders generated by the grating and to spatially filter the reference beam by use of a second pinhole (the reference pinhole), thereby removing the aberrations imparted by the optical system. The test beam, which also contains the aberrations imparted by the optical system, is largely undisturbed by the image-plane mask by virtue of its passing through a window in the PS/PDI mask that is large relative to the diameter of the point-spread function (PSF) of the optical system. The test beam and the reference beam propagate to the mixing plane where they overlap to create an interference pattern recorded on a CCD detector. The recorded interferogram yields information on the deviation of the test beam from the nominally spherical reference beam.

3. Null-Test Description

On the basis of the description above, if the optic under test were perfect (generating a perfect spherical wave), one might expect the recorded interferogram to consist solely of a uniform spatial-frequency fringe pattern, indicating a uniform difference wave front. When examined in greater detail, however, even with a perfect optic there will be deviations from a uniform spatial-frequency fringe pattern simply because of the interferometer geometry. In particular, the image-plane beam separation is responsible for systematic path-length differences. If not compensated, this effect and other geometric effects would limit the accuracy of the PS/PDI.

In practice, the optic under test is not perfect and both beams impinging on the image plane will be aberrated. Because of limitations in the spatial-filtering process responsible for generating the reference wave, the reference wave will contain imperfections that further complicate the measurement.

To measure the effects described above and to calibrate the interferometer, we performed a null test. A natural way to implement a null test for the PS/PDI is to replace the PS/PDI mask with a two-pinhole mask (null mask) [Fig. 1(b)]. In the null mask the large test window is replaced with a second pinhole equivalent in size or smaller than the reference pinhole. These pinholes are usually in the 80–150-nm-diameter range and are chosen to be smaller than the diffraction-limited resolution of the optic under test. Figure 2 shows scanning electron microscope images of a standard PS/PDI mask [Fig. 2(a)] and a null mask [Fig 2(b)]. These masks were fabricated with electron-beam lithography and reactive-ion etching. The masks are made up of a 200-nm-thick nickel absorbing layer evaporated on 100-nm-thick Si_3N_4 membranes. The mask features are etched completely through the membrane prior to the nickel evaporation, leaving the pinholes and windows completely open in the finished masks, thereby maximizing their transmission. With the null mask in place, both the test and the reference beams are spatially filtered, creating two nearly spherical waves. The null mask also contains a 4.5-μm window placed 40 μm below the pinhole pair for alignment purposes.

4. Geometrical Coma Systematic Error

For the EUV PS/PDI with an image-side numerical aperture (NA) less than 0.1, the largest systematic geometric effect is coma, which arises because of the shear between two nominally spherical wave fronts. Interfering two decentered spherical waves gives rise to a hyperbolic fringe field that appears as coma in the reconstructed wave front. We can readily find the magnitude of this coma error analytically by considering the path-length difference from two laterally separated point sources to a point in the mixing (detector) plane (Fig. 3). The lateral point separation,

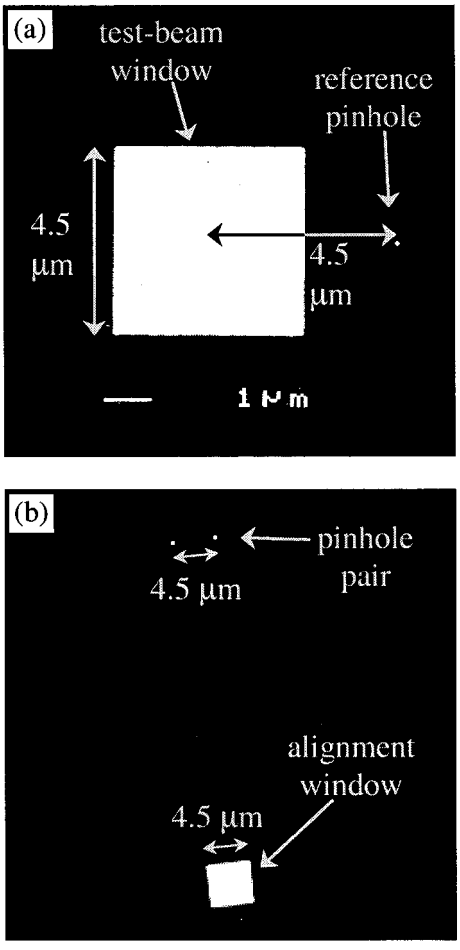

Fig. 2. Scanning electron microscope images of (a) a standard PS/PDI mask and (b) a null mask. The square window in (a) is the test-beam window, and the reference pinhole to the right-hand side has a diameter <100 nm. In (b) we see the pinhole pair (~120-nm diameter each) along with an alignment window ~40 μm below the pinholes.

s, is set equal to the image-point (pinhole) separation in the image plane. Without loss of generality we assume the point separation, s, to lie along the x axis. Expressing r_1 and r_2 (Fig. 3) as second-order binomial expansions and considering the path-length difference ($\Delta r = r_1 - r_2$) as a function of mixing-plane position in polar coordinates (ρ, θ), we obtain

$$\Delta r = \left\{\frac{s}{2z^3}\rho^3 - \left[\frac{s}{z} - \left(\frac{s}{2z}\right)^3\right]\rho\right\}\cos\theta, \tag{1}$$

We note that a first-order expansion of r_1 and r_2 (the Fresnel approximation) is not accurate enough to determine the geometric coma effect being sought here.

Expressing Δr in terms of the Zernike polynomials[11] for coma and tilt, we obtain

$$\Delta r = [C(3\rho^3 - 2\rho) + T\rho]\cos\theta, \tag{2}$$

where C is the coefficient of the Zernike x-direction coma polynomial and T is the coefficient of the Zernike x-direction tilt polynomial. We use the convention in which the Zernike polynomials are bounded by $[-1, 1]$ on the unit circle and where, therefore, the Zernike coefficient magnitudes describe the zero-to-peak excursion of the corresponding polynomial. From Eqs. (1) and (2) we find that the orientation of the geometric coma follows the direction of the image-plane beam separation. The Zernike coefficient magnitude of the geometric coma can be written as

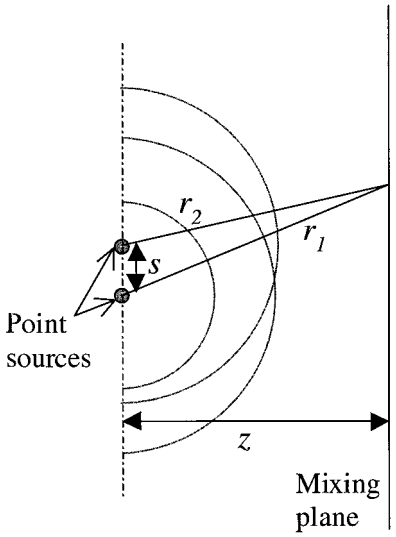

Fig. 3. Measurement geometry leading to systematic coma.

$$C = \frac{s}{6}\left(\frac{r_m}{z}\right)^3, \tag{3}$$

where r_m is the maximum radial (lateral) extent of the measurement in the mixing plane. Equation (3) can be rewritten in terms of the measurement NA and simplified with the small angle approximation, yielding

$$C = \frac{s}{6}\tan^3[\sin^{-1}(\mathrm{NA})] \approx \frac{1}{6}s\,\mathrm{NA}^3, \tag{4}$$

where NA is the variable representing the NA of the measurement.

Figure 4 shows a plot of the theoretical geometric coma as a function of NA. The image-plane beam separation, s, is set to the typical experimental value of 4.5 μm. For current EUV lithographic Schwarzschild testing we are interested in NA's between 0.06 and 0.1. For these values the geometric coma effect limits the uncalibrated interferometer to a measurement accuracy ranging from 0.16 to 0.75 nm. Calibrating the interferometer to remove this geometric coma term is required for achieving the desired measurement accuracy of better than $\lambda/100$ at typical EUV wavelengths (13.5 nm). Noting that the geometric coma term is parallel to the Zernike tilt component of the path-length difference, coma removal involves both determination of the NA of the measurement and the identification of the tilt orientation.

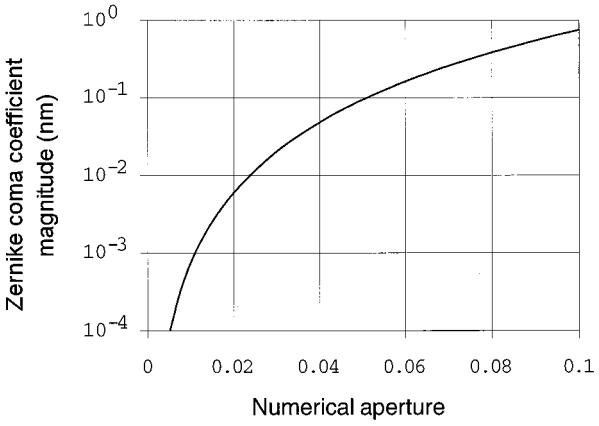

Fig. 4. Geometric-coma-induced error in waves as a function of NA (s = 4.5 μm).

Higher-order expansion of the path-length difference leads to minor corrections to the coma magnitude presented here and to the addition of higher-order coma error terms. For instance, a third-order expansion would lead to terms proportional to NA^5, which are negligibly small for the PS/PDI configuration considered here. For a typical EUV case of s = 4.5 μm and NA = 0.08, the third-order expansion yields a second-order-coma-error magnitude of less than 6.5×10^{-4} nm or λ/20000. These errors can, however, become nonnegligible in higher-NA systems.

5. Detector Misalignment Systematic Effect

Another potential source of geometric measurement error arises from the planar detector alignment with respect to the central ray of the optical system. Proper alignment, as was assumed above, requires the detector plane to be perpendicular to the central ray of the optical system under test. We can consider the effect of misalignment as depicted in Fig. 5 by repeating the analysis above, taking into consideration the x and the y tilt of the mixing plane, γ_x and γ_y, respectively, and again assuming the image-plane point separation to lie along the x axis.

The primary effect of detector tilt is to add astigmatism to the measurement. Also, when the tilt is in the direction parallel to the point separation s, there is an additional defocus error. The path-length error due to detector tilt can be written as

$$\Delta r = \frac{s\rho^2}{2z^2}[\gamma_x(\cos 2\theta + 1) - \gamma_y \sin 2\theta]. \quad (5)$$

From Eq. (5) we find the detector-tilt-induced astigmatism error to have a Zernike coefficient magnitude of

$$e_a \approx \tfrac{1}{2} s\, \mathrm{NA}^2 (y_x^{\,2} + \gamma_y^{\,2})^{1/2} \quad (6)$$

and the tilt-induced defocus error to have a Zernike coefficient magnitude of

$$e_d \approx \tfrac{1}{4} s \gamma_x \mathrm{NA}^2, \quad (7)$$

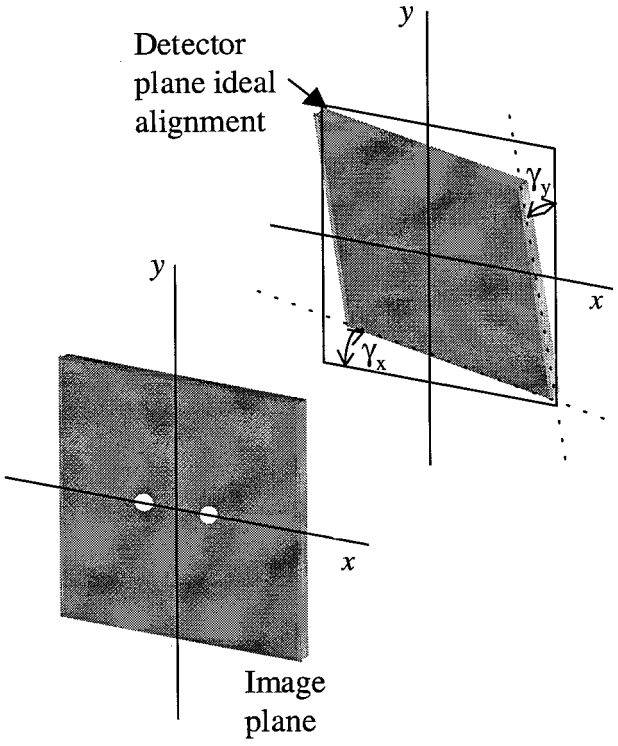

Fig. 5. Geometry for predicting the detector-tilt-induced systematic astigmatism error.

where again we used the small angle approximation to express NA ≈ r_m/z. Considering the typical experimental values of s = 4.5 μm and NA = 0.08, we see the astigmatism error magnitude to be ~0.25 nm (0.019 waves) per degree of detector tilt.

6. Reference-Pinhole-Induced Errors

Reference-pinhole-induced errors are much more subtle than the measurement geometry effects discussed above and are difficult to treat analytically. These errors depend both on the quality of the pinholes and on the quality of the optic under test. The quality of the optic under test plays an important role, because the reference pinhole spatially filters the PSF of the optic to produce the reference beam. The greater the magnitude of the aberrations present in the optic, the more crucial this spatial-filtering process becomes. From this argument we see that it becomes easier to achieve an arbitrary accuracy as the quality of the optics being tested improves.

For convenience, we decompose incomplete spatial filtering by the mask into two components. The first component arises from residual transmission through the absorber comprising the image-plane mask. We subsequently refer to this as *transmission error*. This error is independent of mask position and cannot be reduced through averaging. The second component arises because the pinhole diameter is of finite size, which allows for a finite spatial-frequency bandwidth to pass through. We subsequently refer to this as *spatial-filtering error*. It is reasonable to assume that spatial-filtering errors

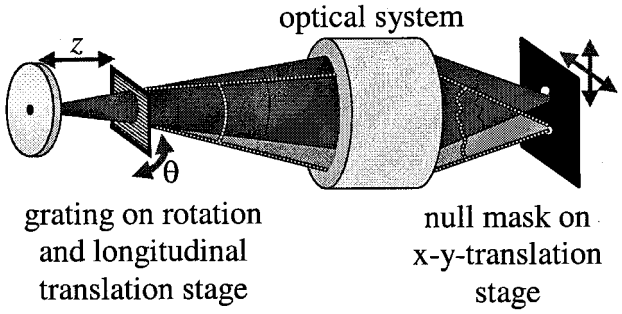

Fig. 6. Critical alignment parameters for the PS/PDI null test.

decorrelate as a function of pinhole position relative to the optic PSF. This allows for the effect of these errors to be mitigated through an averaging process, wherein the pinhole position is slightly changed (a fraction of the optic PSF width) between consecutive measurements.

Another source of reference-pinhole-induced error is defects in the pinhole. These errors can, in principle, be reduced by averaging of measurements from an ensemble of equivalently sized pinholes.

7. Null-Test Alignment

The most difficult aspect of performing the null test at EUV wavelengths is the required image-plane alignment of the two image points onto the two pinholes. Proper alignment is crucial, because it has significant impact on the quality of the diffracted beams. Experience has shown the alignment tolerance required to achieve optimal accuracy from a given pinhole to be of the order of one-tenth the image-point size. For typical EUV lithographic optics this corresponds to an alignment tolerance of 15 nm or smaller. In this section we describe a fast, repeatable, and systematic method for performing the alignment required for implementing the null test.

In the conventional PS/PDI configuration used for optical system testing, the alignment procedure consists primarily of aligning the reference beam to the reference pinhole. A set of tools simplifying this alignment procedure is described elsewhere.[6] Because the test-beam window is large relative to the image-point size and is on par with the image-point separation, the exact separation and rotational orientation of the two image points is not critical. However, for the null-test alignment we must simultaneously align two image points to two pinholes. In this case image-point separation and orientation become crucial, making alignment significantly more challenging.

The orientation angle of the image points is determined by the orientation of the grating pattern, described by an azimuthal angle θ in Fig. 6. For a grating of a given pitch, the separation of the points is determined by the distance between the grating and the object pinhole, z in Fig. 6. The separation of the pinholes is set during fabrication of the null mask, and orientation of the pinholes is determined during installation. To achieve alignment, we require rotation and longitudinal-position control of the grating.

Our conventional alignment techniques work by interactive optimization of the interferometric fringe pattern while the alignment parameters are varied. This process would be prohibitively difficult in the null-test case, owing to the large number of alignment parameters. The technique described here overcomes this problem by decomposing the alignment problem into four independent steps, thereby greatly reducing the parameter space for each step. The first two steps of this method involve independently measuring the image points and pinholes in orientation and separation relative to a fixed reference coordinate system. This reference coordinate system is most conveniently the stationary CCD detector located after the image plane. The third step is to use the grating stage to modify the orientation and the separation of the image-point pair so as to match that measured for the pinhole pair. Finally, the fourth step is to align the pinhole pair to the image-point pair in the two remaining parameters (x, y) by translation of the image-plane mask with a nanometer-resolution stage.

To measure the orientation and the separation of the image-point and pinhole pairs relative to the CCD, interferometric techniques are used. We begin by considering the measurement of the image-point pair. The image-point separation and orientation can be measured by recording of the fringe pattern produced in the absence of the image-plane mask. Because it is impractical to remove and accurately replace the image-plane mask, it is desirable to measure this fringe pattern with the mask in place. This can be accomplished with a partially transparent mask. The 200-nm-thick nickel absorber masks currently in use for EUV PS/PDI meet this criterion. Transmission through these masks at a wavelength of 13.5 nm, however, is less than 10^{-6}. Therefore care must be taken to design a mask that has sufficiently large feature-free areas such that the transmitted-light fringes can be observed relative to scattered light propagating through open mask areas such as alignment windows. To observe the *transmission-fringe pattern*, the mask is positioned such that the image-point pair falls onto a feature-free region of the mask. This positioning is achieved with the image-plane stage.

An alternative to using a partially transmitting mask is to use a mask with special alignment features allowing for the grating-based fringes to be measured. These alignment features could, for example, be a pair of windows that are large relative to the PSF of the optic under test and have a center-to-center separation equal to the pinhole separation.

The next step in the alignment procedure is to measure the orientation and the separation of the pinhole pair. In this case the mask is positioned such that the image-point pair falls close enough to the pinhole pair to allow for fringes produced by pinhole-diffracted light to be observed. To achieve

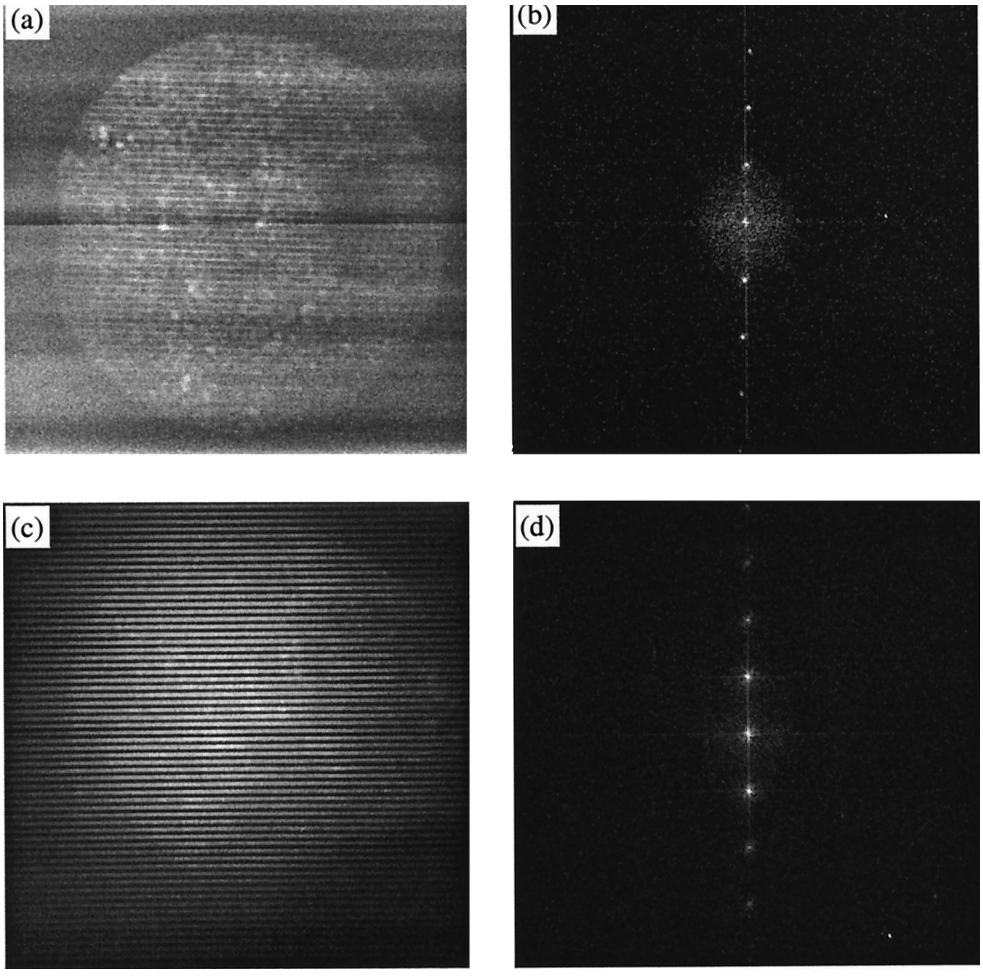

Fig. 7. Demonstration of the null-test alignment technique. (a) Transmission-fringe pattern through membrane and (b) its Fourier transform. (c) Two-pinhole-fringe pattern and (d) its Fourier transform.

this positioning, we locate the large alignment window [Fig. 2(b)] through a coarse scanning process and translate a known distance to the pinhole pair. Because we are using the *two-pinhole-fringe pattern* in an alignment technique whose goal is to align the image-point pair to the pinhole pair, we must consider the question of capture tolerance: How close must the initial relative orientation and separation be to enable this method? This capture range is determined primarily by the optic PSF. For a typical EUV PS/PDI configuration and an assumed PSF size of 150 nm, the capture tolerances are $\sim 1.2°$ for the grating orientation and 1.5 mm for the grating-to-entrance-pinhole separation. The distance from the grating to the entrance pinhole is nominally 60 mm. With careful assembly these capture tolerances are readily achieved.

Another important question is how to distinguish between a transmission-fringe pattern and a two-pinhole-fringe pattern; the two-pinhole-fringe pattern is easily recognized, because it appears outside the NA of the optic under test. In the PS/PDI the reference pinhole size is always chosen to be significantly smaller than the diffraction-limited resolution limit of the optic under test; hence the pinhole diffraction pattern extends beyond the system NA.

Having measured the separation and the orientation of both the image-point and the pinhole pairs, we can now determine the adjustments required for the grating position and orientation. In practice, complete alignment requires several iterations of the procedure described above.

Figure 7 demonstrates this alignment technique. Figure 7(a) shows a representative transmission-fringe pattern. The signal level is extremely low owing to the high attenuation of the mask. The fringes are limited to the area of the optic exit pupil. Figure 7(b) shows the Fourier transform of the fringe pattern revealing the two-dimensional carrier frequency, and hence the spatial frequency and orientation of the fringes. The rotation of the grating relative to the CCD is evident. Figure 7(c) shows a representative two-pinhole-fringe pattern prior to alignment. The fringes are now seen to extend nearly to the edges of the CCD, beyond the NA of the optic under test as seen by the outline of the exit pupil in Fig. 7(a). Figure 7(d) shows the Fourier transform, again revealing the two-dimensional carrier,

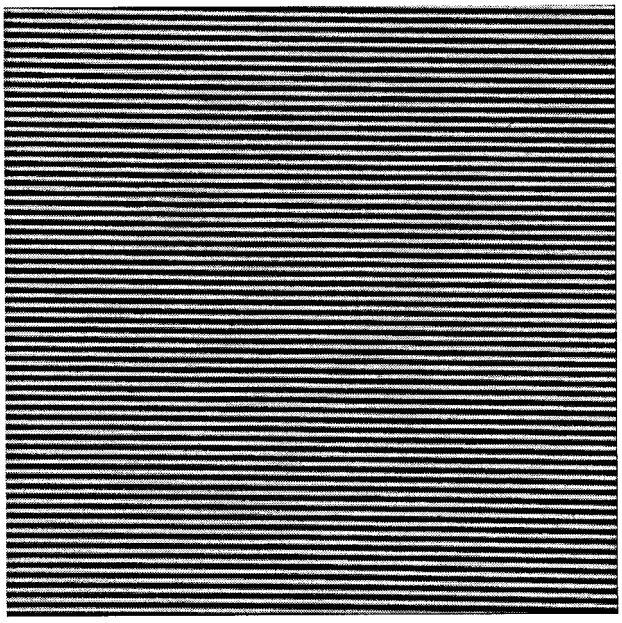

Fig. 8. Representative null-test interferogram with a 100-nm-pinhole null mask and a wavelength of 13.5 nm (full 1-in.^{2} CCD image, 512 × 512 pixels).

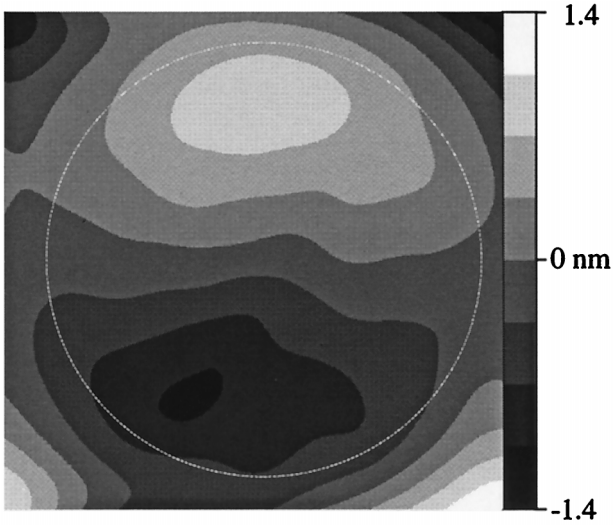

Fig. 9. Reconstructed wave front from interferogram in Fig. 6 quantized to 8 gray levels.

which here represents the pinhole orientation and separation. The pinholes are well aligned to the CCD. From these interferograms and the known geometry of the system we can determine the corrections required for the orientation and the longitudinal position (θ and z, respectively) of the grating. Figure 8 shows the two-pinhole-fringe pattern after implementation of this correction. The significant improvement over the two-pinhole-fringe pattern obtained with only capture-tolerance alignment [Fig. 7(c)] is evident.

The accuracy of this alignment technique is limited by uncertainty in the measurement of the interferometric tilt terms. A repeatability test has experimentally demonstrated a beam separation measurement uncertainty of 3.3 nm (3σ) for the two-pinhole-fringe pattern and 0.9 nm (3σ) for the transmission-fringe pattern, yielding an alignment accuracy of 3.4 nm (3σ).

8. Experimental Results

The accuracy of the PS/PDI has been experimentally characterized in a configuration designed to test EUV 10×-demagnification Schwarzschild optics.[12] The objective used is designed to operate at a wavelength near 13 nm and has a rms wave-front error of 0.16 waves ($\lambda/6$ or 2.2 nm) in the full-measurement bandwidth over a NA of 0.08. It should be noted that this optic was fabricated several years ago and has particularly poor wave-front quality when compared with current state-of-the-art objectives with wave-front aberrations below 0.05 waves ($\lambda/20$ or 0.7 nm) rms.[13]

For null-test alignment purposes, the interferometer grating stage was modified to enable *in situ* adjustment of the grating orientation and longitudinal position while sacrificing the phase shifting capability. Because the PS/PDI is an off-axis-reference interferometer, however, the fringe analysis is readily implemented with static-fringe Fourier methods.[14] A variety of null masks with various pinhole sizes were used including the 120-nm pinhole null mask shown in Fig. 2(b). The pinhole separation in each case was 4.5 μm. The object pinhole was a 0.5-μm laser-drilled pinhole, one-half the diffraction-limited resolution on the object side. The interferometry was performed with an undulator beamline[15] at the Advanced Light Source synchrotron radiation facility at Lawrence Berkeley National Laboratory. The beamline provides a tunable source of effectively coherent EUV radiation.[16] The tests were performed at a wavelength of 13.5 nm with a bandwidth, $\lambda/\Delta\lambda$, of approximately 350.

Figure 8 shows a null-test interferogram recorded on an EUV CCD with a 100-nm-pinhole null mask. The full 1-in.^{2} (~6.45-cm^2) CCD area is shown; the image has been intensity equalized to reveal the quality of the fringes all the way to the edges of the CCD. The wave-front phase representing the path-length difference is recovered from the interferogram by use of the Fourier-transform method of fringe-pattern analysis.[14] With tilt removed the wave front is shown in Fig. 9. As expected, the dominant term is coma in the direction of the pinhole separation. Analysis of the wave front over a 0.082-NA circular subaperture (depicted by the dotted outline in Fig. 9) shows the magnitude of the coma to be 0.029 waves (0.39 nm) zero to peak or 0.010 waves (0.13 nm) rms. The measurement NA is chosen to be slightly larger than the design NA of the Schwarzschild system.

To separate the systematic and the random effects, the measurement was repeated 20 times with intentional, arbitrary displacements of the pinhole pair between measurements. Displacements were limited to less than 25 nm from the nominal position.

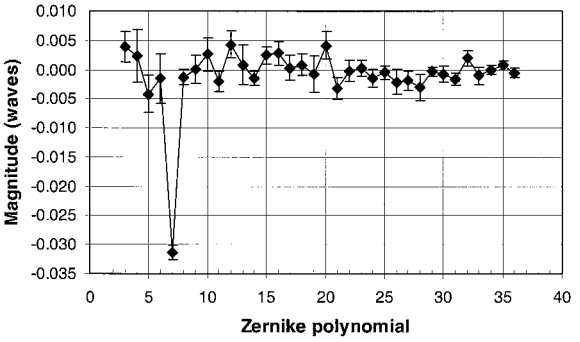

Fig. 10. Average and standard deviation of Zernike-polynomial fit from 20 independent measurements.

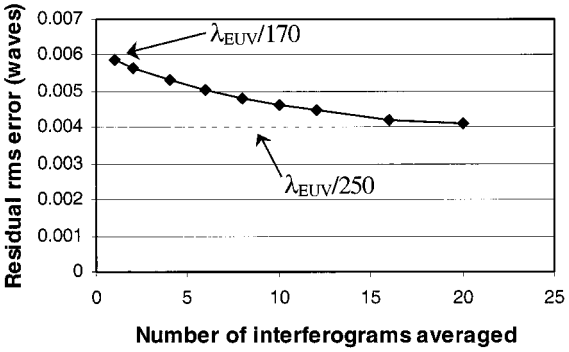

Fig. 11. Residual rms error after removal of predicted geometric coma term as a function of wave-front averaging.

Figure 10 shows a plot of the average of the Zernike-polynomial fit coefficients determined for the 20 individual wave fronts. The error bars represent plus and minus 1 standard deviation of the 20 individual Zernike-polynomial fit coefficients. We note that the numbering convention used here is as follows (0, 1, 2, 3, 4, 5, 6, 7, 8, . . .) = (piston, x-tilt, y-tilt, defocus, 0°-astigmatism, 45°-astigmatism, x-coma, y-coma, spherical, higher-order terms).

As shown in Fig. 10, the dominant term in the Zernike-polynomial fit is coma in the direction of the pinhole separation. The average value of the coma coefficient has a magnitude of 0.0314 ± 0.0012 waves (0.424 ± 0.016 nm). Using Eq. (4) with a measurement NA of 0.082 and a pinhole separation, s, of 4.5 μm, we find the predicted geometric coma magnitude to be 0.0306 waves (0.413 nm). The average measured coma matches the prediction to within the measurement precision of 0.0012 waves (0.016 nm).

Removing the predicted geometric coma term from the wave front in Fig. 9, we find the rms magnitude of the residual wave front to be 0.0050 waves (λ/200 or 0.068 nm). The expected accuracy of a single measurement, however, should be taken as the average residual rms magnitude from the set of 20 independent measurements. Performing this average yields a single-interferogram accuracy of 0.0059 ± 0.0011 waves rms (λ/169 or 0.080 nm). This accuracy can be taken as the systematic-plus-random-error-limited accuracy. However, as noted above, the random-error term can be reduced through averaging, thereby improving the accuracy of the measurement. The plot in Fig. 11 shows the residual wave-front rms magnitude (after removal of the predicted geometric coma) as a function of the number of measurements averaged. As expected, the accuracy improves with averaging and reaches 0.0041 ± 0.0003 waves (λ/244 or 0.055 nm) rms. We take this to be the systematic-error-limited accuracy of the reference wave front. Because the systematic- and random-error terms add in quadrature, we see the random-error contribution to the single-measurement accuracy to be 0.0042 waves rms. This value can also be viewed as the single-measurement reference-wave-limited precision. Figure 12 shows the average wave front prior to and after removal of the geometric coma.

Considering only Zernike-polynomial terms through 36 (the set typically used to describe wave-front figure error), yields a systematic-error-limited accuracy of 0.0037 ± 0.0003 waves (λ/270 or 0.050 nm) rms.

In addition to the geometric coma effect, detector tilt was identified as a systematic error source. Examining the astigmatism and defocus terms from the average Zernike-polynomial fit in Fig. 10, we draw conclusions about the presence of detector-tilt-induced error. For detector tilt in the direction of the image-plane beam separation we expect the mean amplitudes of Zernike polynomials 3 and 4 to be similar [Eq. (5)]. Figure 10 shows these two terms to have mean amplitudes of 0.0039 and 0.0024 waves, respectively. Given the relatively large error bars (±0.003 and ± 0.005 for terms 3 and 4, respectively), it is not possible to conclusively attribute the measured astigmatism to detector-tilt-induced effects. We draw the same conclusion for Zernike polynomial 5, the astigmatism term linked to tilt perpendicular to the image-plane beam separation. Astigmatism due to detector-tilt-induced effects is limited to a magnitude below 0.005 waves (0.07 nm). This suggests that the detector-tilt alignment is correct to better than 4 mrad, a reasonable value for standard machining techniques. We note that a dual-orientation measurement configuration, wherein the null test is repeated with a rotation of the pinholes, could help separate low-level measurement-geometry-based systematic effects from systematic errors due to incomplete spatial filtering of the optic aberrations. Also, a test in which the detector tilt can be changed *in situ* could be used to isolate the tilt-error-induced astigmatism.

A null test similar to the null test described above was also performed with 80-nm pinholes. In this case the mask absorber thickness was increased to 240 nm to prevent the residual transmission from dominating the pinhole-diffracted light. Figure 13 shows an interferogram from the measurement, and Fig. 14 shows the average wave front (11 independent measurements) prior to and after removal of the geometric coma. The measured coma is 0.0313 ±

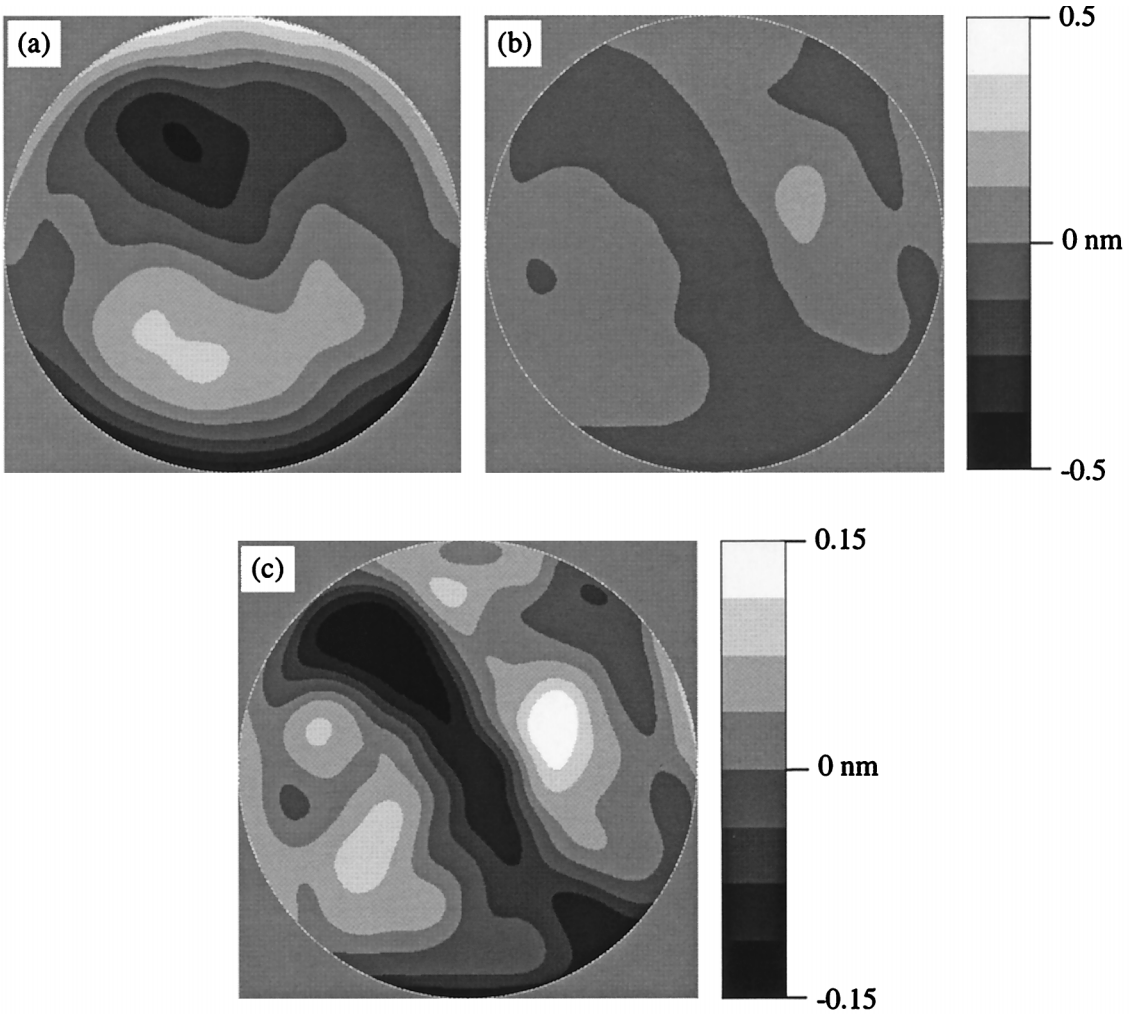

Fig. 12. Average 100-nm-pinhole wave front displayed as 8-level gray scale: (a) prior to predicted geometric coma removal and (b) after predicted geometric coma removal. (c) Rescaled version of (b) to accentuate the wave-front structure. The rms error of wave front in (b) and (c) is 0.0041 waves ($\lambda/244$ or 0.055 nm).

0.0004 waves, and the residual average-wave-front error after removal of the predicted geometric coma (the systematic-error-limited accuracy) is 0.0028 ± 0.0001 waves ($\lambda/357$ or 0.038 nm) rms. The single-measurement accuracy for the 80-nm pinhole case is 0.0039 ± 0.0004 waves ($\lambda/256$ or 0.053 nm) rms. Furthermore, the 36-Zernike-polynomial systematic-error-limited accuracy was measured to be 0.0023 ± 0.0001 waves ($\lambda/435$ or 0.031 nm) rms.

Null tests were also performed with 120- and 140-nm pinholes. Measured accuracies and geometric coma terms are presented in Tables 1 and 2, respectively.

9. Discussion

A. Null-Test Limitations

Because all significant geometric effects were accounted for, we expect the measured residual error presented in Section 8 to be the result of reference-pinhole-induced errors and measurement noise. We

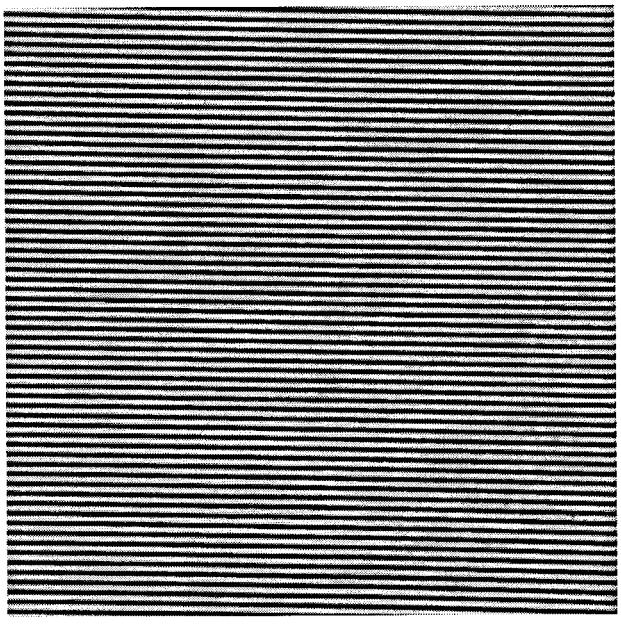

Fig. 13. Representative null-test interferogram with a 80-nm-pinhole null mask and a wavelength of 13.5 nm (full 1-in.^{2} CCD image, 512 × 512 pixels).

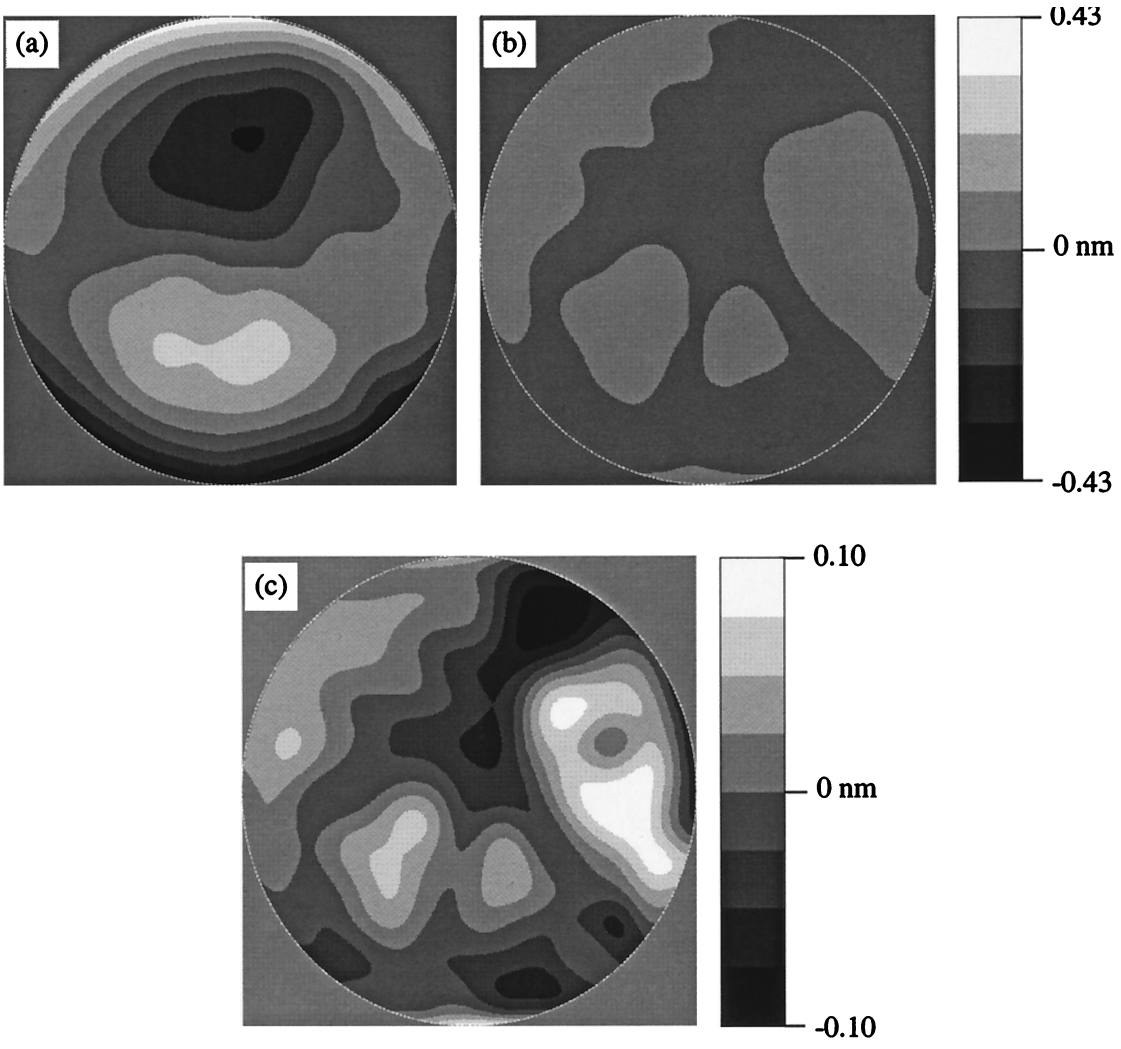

Fig. 14. Average 80-nm pinhole wave front displayed as 8-level gray scale: (a) prior to predicted geometric coma removal and (b) after predicted geometric coma removal. (c) is a rescaled version of (b) to accentuate the wave-front structure. The rms error of wave front in (b) and (c) is 0.0028 waves ($\lambda/357$ or 0.038 nm).

therefore consider the sensitivity of the null test to reference wave-front aberrations.

It is evident that the null test is a difference measurement between two, laterally sheared, independent realizations of the reference wave. This implies that it does not provide a true measure of either wave individually. The sensitivity of the null test depends on the characteristics of the reference waves. When the two waves are uncorrelated, the null test will on average yield an accuracy result that is worse than the true accuracy; thus it is a conservative measurement for uncorrelated errors. However, when the two waves are correlated, and the shear is small relative to the wave-front aberrations, the null test will yield an accuracy result that is deceptively better than the true accuracy.

Because the transmission component of reference-pinhole-induced errors (see Section 6) is correlated between the two interfering beams, the null test is not well suited to measuring it. In practice, however, transmission errors are extremely small, and this limitation does not restrict the utility of the null

Table 1. Reference-Wave rms Accuracy as a Function of Null-Mask Pinhole Size

Pinhole Size (nm)	Systematic-Error-Limited rms Accuracy (Waves)	Systematic-Plus-Random-Error-Limited rms Accuracy (Waves)
140	0.012 ± 0.001 (0.16 nm or $\lambda/83$)	0.014 ± 0.002 (0.19 nm or $\lambda/71$)
120	0.010 ± 0.001 (0.14 nm or $\lambda/100$)	0.011 ± 0.001 (0.15 nm or $\lambda/91$)
100	0.0041 ± 0.0003 (0.055 nm or $\lambda/244$)	0.0059 ± 0.0011 (0.080 nm or $\lambda/169$)
80	0.0028 ± 0.0001 (0.038 nm or $\lambda/357$)	0.0039 ± 0.0004 (0.052 nm or $\lambda/250$)

Table 2. Measured Coma and Measured Coma Error Relative to Predicted Value as a Function of Null-Mask Pinhole Size

Pinhole Size (nm)	Measured-Coma Magnitude (Waves)	Coma Error Relative to Predicted Coma Magnitude (Waves)
140	0.021 ± 0.002 (0.28 nm)	0.010 (0.13 nm or λ/100)
120	0.025 ± 0.007 (0.34 nm)	0.006 (0.08 nm or λ/167)
100	0.0314 ± 0.0012 (0.424 nm)	0.0008 (0.011 nm or λ/1250)
80	0.0313 ± 0.0004 (0.423 nm)	0.0007 (0.010 nm or λ/1428)

test. Transmission errors can be viewed as the addition of an attenuated version of the test-beam wave front to the pinhole-diffracted wave front. The attenuated test-beam wave front causes small perturbations to the diffracted wave front. The phase component of this perturbation can be shown to be limited to the amplitude ratio of the transmitted and the diffracted light.

Considering the 80-nm-pinhole case described above (240-nm nickel absorber), this ratio leads to an expected transmission error component of less than 2.6×10^{-4} waves (λ/3800 or 0.0035 nm).

It is also important to note that the null test presented here characterizes errors originating at or after the image plane. Systematic errors introduced before the image plane (for example, from the illumination of a planar uniform-pitch grating with a spherical wave) may be assessed by other means. These preimage-plane geometric errors have, however, been shown to be small compared with those measured by the null test.[6] Another potential source of preimage-plane error is the object pinhole, which generates the illumination wave by diffraction. The object-pinhole quality can be quantified by use of similar two-pinhole tests. Because the optical systems being tested are typically demagnifying systems, the object-pinhole requirements are generally less severe than for the image-plane pinhole.

B. Null-Test Relevance to Actual Phase-Shifting Point-Diffraction Interferometer Measurements

To prevent grating-line-placement errors from coupling to the test beam, the PS/PDI was in the past typically implemented with the zero order of the grating as the test beam and the first-diffracted order as the pinhole-filtered-reference beam (the *first-order-reference* configuration). Because at EUV wavelengths we are generally restricted to using amplitude gratings, this configuration can at best provide a one-to-one reference-to-test-beam power ratio as defined prior to the filtering loss induced by the image-plane pinhole. When high accuracy is sought and small pinholes are used, this filtering loss becomes significant, leading to a large power mismatch between the two beams in the mixing plane. This mismatch gives rise to interferograms of low contrast that are susceptible to effects such as photon noise and detector-quantization noise.

When the optic used in the null tests presented here was tested in the conventional PS/PDI configuration, it was found that pinholes of sizes 100 nm and smaller yielded intolerably low fringe contrast in the first-order-reference configuration. Therefore, in practice we were limited to the measurement accuracy of λ/100 provided by 120-nm pinholes.

Because grating-line-placement errors have been found to be significantly smaller than λ/100, it is actually beneficial to reverse the beams used as the reference and the test waves. In this *zero-order-reference* configuration, arbitrarily high reference-to-test-beam power ratios can be achieved by use of binary gratings with duty cycles other than 50%. In principle, the grating duty cycle can be chosen to exactly balance the filtering loss, which depends both on the aberrations in the test optic and on the size of the reference pinhole. This zero-order-reference configuration is now routinely used during testing of optics, enabling the use of 100-nm and smaller pinholes. Measurements have shown the grating-induced error in the zero-order-reference configuration to be approximately λ/330 (the gratings used were fabricated by electron-beam lithography). Furthermore, assuming the line-placement errors to be uncorrelated over large displacements of the grating, the effective accuracy can be improved through an averaging process. In the case presented here, we clearly benefit from reversing the beam order and using smaller reference pinholes.

We note also that using phase gratings it is possible to both achieve an arbitrarily high reference-to-test-beam power ratio and to use the diffracted beam as the reference. We are currently investigating fabrication techniques for EUV phase gratings.

The measurements presented here were performed by use of an optic with a rms wave-front error that is three times larger than current state-of-the-art EUV optics fabrication. When limited by errors induced by incomplete spatial filtering, as is believed to be the case here, the accuracy of the PS/PDI is expected to improve with the quality of the optics under test. Therefore the systematic measurement errors presented here are expected to be an upper bound on the errors present during testing of newer, higher-quality optics.

The authors are greatly indebted to Erik Anderson for nanofabrication of masks and gratings, to Phil Batson for engineering support, and to the entire Center for X-Ray Optics staff for enabling this research. We also acknowledge valuable discussions with Edita Tejnil and Hector Medecki. Special thanks are due to Paul Denham for expert assistance with experimental control systems. This research was supported by the EUV Limited Liability Com-

pany, the Semiconductor Research Corporation, the Defense Advanced Research Projects Agency, and the Department of Energy Office of Basic Energy Science.

References

1. J. H. Underwood and T. W. Barbee, Jr., "Layered synthetic microstructures as Bragg diffractors for X rays and extreme ultraviolet: theory and predicted performance," Appl. Opt. **20,** 3027–3034 (1981).
2. D. M. Williamson, "The elusive diffraction limit," in *Extreme Ultraviolet Lithography*, F. Zernike and D. T Attwood, eds., Vol. 23 of OSA Proceedings Series (Optical Society of America, Washington, D.C., 1995), pp. 68–76.
3. H. Medecki, E. Tejnil, K. A. Goldberg, and J. Bokor, "Phase-shifting point diffraction interferometer," Opt. Lett. **21,** 1526–1528 (1996).
4. E. Tejnil, K. A. Goldberg, S. H. Lee, H. Medecki, P. J. Batson, P. E. Denham, A. A. MacDowell, J. Bokor, and D. Attwood, "At-wavelength interferometry for EUV lithography," J. Vac. Sci. Technol. B **15,** 2455–2461 (1997).
5. K. A. Goldberg, E. Tejnil, S. H. Lee, H. Medecki, D. T. Attwood, K. H. Jackson, and J. Bokor, "Characterization of an EUV Schwarzschild objective using phase-shifting point diffraction interferometry," in *Emerging Lithographic Technologies*, D. E. Seeger, ed., Proc. SPIE **3048,** 264–270 (1997).
6. K. A. Goldberg, "Extreme ultraviolet interferometry," Ph.D. dissertation (University of California, Berkeley, Berkeley, Calif., 1997).
7. J. E. Bjorkholm, A. A. MacDowell, O. R. Wood II, Z. Tan, B. LaFontaine, and D. M. Tennant, "Phase-measuring interferometry using extreme ultraviolet radiation," J. Vac. Sci. Technol. B **13,** 2919–2922 (1995).
8. A. K. Ray-Chaudhuri, W. Ng, F. Cerrina, Z. Tan, J. Bjorkholm, D. Tennant, and S. J. Spector, "Alignment of a multilayer-coated imaging system using extreme ultraviolet Foucault and Ronchi interferometric testing," J. Vac. Sci. Technol. B **13,** 3089–3093 (1995).
9. W. Linnik, "A simple interferometer to test optical systems," Proc. P. N. Lebedev Phys. Inst. **1,** 210–212 (1933).
10. R. N. Smartt and W. H. Steel, "Theory and application of point-diffraction interferometers," Jpn. J. Appl. Phys. **14,** Suppl. 14–1, 351–356 (1975).
11. A. Bathia and E. Wolf, "The Zernike circle polynomials occurring in diffraction theory," Proc. Phys. Soc. London Sect. B **65,** 909–910 (1952).
12. D. A. Tichenor, G. D. Kubiak, M. E. Malinowski, R. H. Stulen, S. J. Haney, K. W. Berger, R. P. Nissen, R. L. Schmitt, G. A. Wilkerson, L. A. Brown, P. A. Spence, P. S. Jin, W. C. Sweat, W. W. Chow, J. E. Bjorkholm, R. R. Freeman, M. D. Himel, A. A. MacDowell, D. M. Tennant, O. R. Wood II, W. K. Waskiewicz, D. L. White, D. L. Windt, and T. E. Jewell, "Development and characterization of a 10× Schwarzschild system for SXPL," in *Soft-X-Ray Projection Lithography,* A. M. Hawryluk and R. H. Stulen, eds., Vol. 18 of OSA Proceedings Series (Optical Society of America, Washington, D.C., 1993), pp. 79–82.
13. K. A. Goldberg, P. Naulleau, S. Lee, C. Chang, C. Bresloff, R. Gaughan, H. Chapman, J. Goldsmith, and J. Bokor, "Direct comparison of EUV and visible-light interferometries," in *Emerging Lithographic Technologies III*, Y. Vladimirsky, ed., Proc. SPIE **3676,** 635–642 (1999).
14. M. Takeda, H. Ina, and S. Kobayashi, "Fourier-transform method of fringe-pattern analysis for computer-based topography and interferometry," J. Opt. Soc. Am. **72,** 156–160 (1982).
15. R. Beguiristain, J. Underwood, M. Koike, P. Batson, E. Gullikson, K. Jackson, H. Medecki, and D. Attwood, "High flux undulator beam line optics for EUV interferometry and photoemission microscopy," in *High Heat Flux Engineering III*, A. M. Khounsary, ed., Proc. SPIE **2855,** 159–169 (1996).
16. D. Attwood, G. Sommargren, R. Beguiristain, K. Nguyen, J. Bokor, N. Ceglio, K. Jackson, M. Koike, and J. Underwood, "Undulator radiation for at-wavelength interferometry of optics for extreme-ultraviolet lithography," Appl. Opt. **32,** 7022–7031 (1993).